ACS APPLIED MATERIALS & INTERFACES

www.acsami.org

Research Article

Transition Metal Tunes Molecular Self-Assembly in Living Cells for Controlling Cell−Cell Crosstalk

Published as part of ACS Applied Materials & Interfaces special issue "Peptide Self-Assembly and Materials".

Xuejiao Yang, Feili Zhang, Bihan Wu, Juan Liang, Laicheng Zhou, Honglei Lu, Zhaoqianqi Feng,* and Huaimin Wang*

Cite This: *ACS Appl. Mater. Interfaces* 2025, 17, 45569−45578

Read Online

ACCESS | Metrics & More | Article Recommendations | Supporting Information

ABSTRACT: This work reports a robust and versatile strategy for harnessing cell-compatible transition metal catalysts to tune peptide self-assembly precisely in living cells. The engineered cell-compatible **Ru catalyst** targets cell membranes by chemically tagging membrane-affinity groups and functionalizing the surfaces of living mammalian cells. The anchored **Ru catalyst** on the cell surface can then recognize the designed substrate and induce the self-assembly of peptides *in situ* through olefin metathesis. Labeling the $CD8^+$ T cells and cancer cells orthogonally with the **Ru catalyst** and peptide substrate can detect the molecular transfer from cancer to immune cells. This work, for the first time, provides a general approach and a versatile technology for generating artificial structures of peptides by abiotic catalysts in living cells.

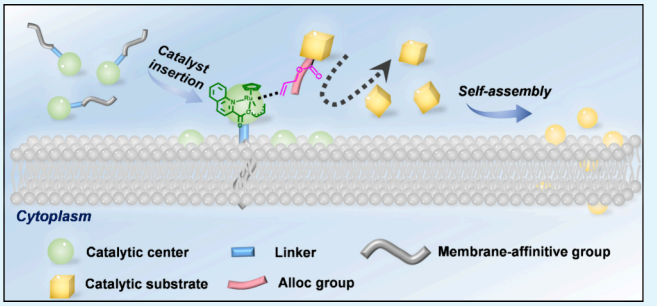

KEYWORDS: *Ru catalyst, peptide, self-assembly, olefin metathesis, material transport*

INTRODUCTION

The biological system employs various stimuli to dictate myriad reactions, forming high-order assemblies (e.g., protein, DNA, and lipid rafts) with sophisticated control and maintaining cell homeostasis.[1−3] *In situ* self-assembly, controlled under local stimuli, is widely used in living systems to build functional structures such as microtubules, actin filaments, and inflammasomes. Inspired by the natural system, *in situ* self-assembly by harnessing microenvironmental differences between normal and diseased cells for cancer therapy, imaging, organelle targeting, and tissue engineering has received increased attention.[4−25] To initiate *in situ* self-assembly, one suitable stimulus or multiple stimuli must be explicit in the biological system. For example, several distinct stimuli of diseased cells, including enzyme, pH, ionic strength, and redox conditions, have successfully triggered molecular self-assembly in living cells.[7,8] However, these approaches suffer from biologically restricted conditions and need to consider meticulous considerations, such as cell types, activate sites, local pH, and expression levels. We consider whether cells of interest can be chemically programmed with biocompatible catalysts under spatiotemporal control to enable *in situ* self-assembly, thereby overcoming biophysical environmental restrictions on stimuli-induced self-assembly in target organelles.

To achieve the above hypothesis, we began with transition metal catalysts and found that ruthenium derivatives could be used to promote intracellular reactions without compromising their catalytic activity.[26−33] We designed two **Ru catalysts** modified with a hydrophobic alkyl chain and cholesterol, respectively. These modifications facilitate the anchoring of **Ru catalysts** at the cell membrane (Scheme 1A). Subsequently, upon incubation of cells with the catalytic substrate, the Alloc group undergoes cleavage by the **Ru catalyst**, leading to the self-assembly of residues into uniform nanospheres surrounding the cell membrane, giving rise to strong fluorescence (Scheme 1B).

After demonstrating the versatility of our strategy to anchor **Ru catalyst** on different types of cells for inducing peptide self-assembly, we also show that orthogonally labeling two cell lines, $CD8^+$ T cells, and cancer cells with **Ru catalyst** and substrate, can detect the materials transport from one cell line to another cell line by a catalytic reaction. As the first report on harnessing transition metal catalysts for tuning the *in situ* self-assembly of peptides in living cells, this work illustrates a fundamentally new methodology for generating activated cells for constructing functional structures.

Received: June 1, 2025
Revised: July 18, 2025
Accepted: July 21, 2025
Published: July 30, 2025

https://doi.org/10.1021/acsami.5c10736
ACS Appl. Mater. Interfaces 2025, 17, 45569−45578

Scheme 1. (A) Molecular Structure of Ru Catalyst (Ru−C_{12}, Ru-Cholesterol) and Catalytic Substrate (NBD-Alloc) and (B) Schematic Illustration of Ru Catalyst Mediated Peptide Self-Assembly on Cell Membrane

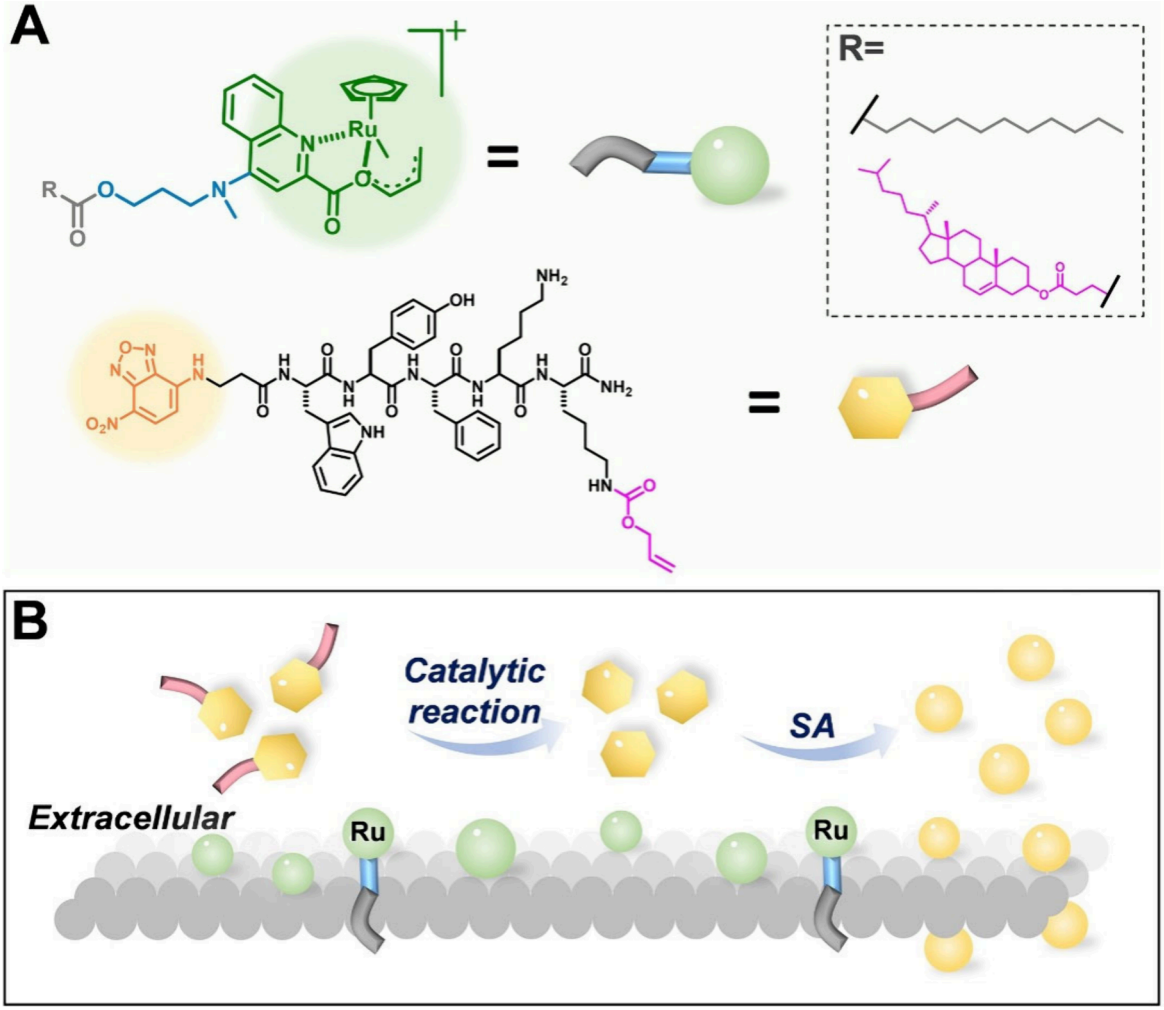

METHODS AND MATERIALS

Experiment Materials and Instruments. All chemicals were purchased from commercial sources and used without further purification. Rink amide resin (0.94 mmol/g) and Fmoc-amino acids were obtained from GL Biochem (Shanghai, China). Other chemical reagents and solvents were purchased from Aladdin Industrial (Shanghai, China). McCoy's 5A medium, Dulbecco's modified eagle medium (DMEM), fetal bovine serum (FBS), live cell imaging solution, Hoechst 33342, membrane deep red tracker, and lysosome deep red tracker were obtained from Gibco (Thermal Fisher Scientific, US).

All cells were cultured in a 5% CO_2 incubator at 37 °C. All mice were obtained from Westlake University Animal Center and maintained in sterile conditions. Animal experiments were approved by the Animal Care and Use Committee of Westlake University and were conducted under the institutional guidelines (license number: AP#22-050-WHM-3).

Synthesis of Ru−C_{12} Catalyst. C_{12}−COOH (30 mg, 0.15 mmol) and Compound A (44.9 mg, 0.15 mmol, 1.0 equiv.) were dissolved in DMF, and then we added EDC (27.9 mg, 0.18 mmol, 1.2 equiv.) and 4-DMAP (3.7 mg, 0.03 mmol, 0.2 equiv.) into the mixture. After stirring at room temperature overnight, we concentrated the mixture by rotary evaporator, then purified **Compound A-C_{12}** using analytic HPLC equipped with C18 column. The [$RuCp(CH_3CN)_3PF_6$] (II) complex (0.45 mg, 1.04 μmol) was dissolved in 1 mL of dry DCM. **Compound A-C_{12}** (0.5 mg, 1.04 mmol, 1.0 equiv.), dissolved in 1 mL of dry DCM, was then placed in the flask under a nitrogen atmosphere. The mixture was stirred at room temperature overnight, after which the product was dried under N_2 and used as a catalyst in the subsequent experiment (Scheme S1).

Synthesis of NBD-Alloc. The reaction proceeded under the protection of N_2. β-Alanine (0.49 g, 5.5 mmol, 1.1 equiv.) and K_2CO_3 (1.52 g, 11 mmol, 2 equiv.) were dissolved in 15 mL of ddH_2O. After being fully dissolved, the NBD-Cl (1 g, 5 mmol, 1 equiv.) dissolving in 40 mL of CH_3OH was added into the above solution dropwise, and the mixture was stirred at 25 °C over 5 h. As the reaction proceeded, the color of solution changed from brown to black, then the resultant solution was concentrated in vacuum and resuspended in 15 mL of ddH_2O. The above mixture was acidified to pH 3.0 with 1 M HCl. After extracting with diethyl ether, we collected the organic phase and concentrated in vacuum. The product was obtained as a brown solid without further purification (1.15 g, 91.3%). We obtained **NBD-Alloc** by standard solid phase peptide synthesis (SPPS) using rink amide resin. The yield was about 80% (Scheme S2).

Synthesis of Compound A-Cholesterol. Compound A (50.0 mg, 0.10 mmol) and cholesteryl hemisuccinate (30.8 mg, 0.10 mmol, 1 equiv.) were dissolved in DMF, and then EDC (19.1 mg, 0.12 mmol, 1.2 equiv.) and 4-DMAP (2.4 mg, 0.02 mmol, 0.2 equiv.) were added into mixtures, and the resultant mixtures were stirred at room temperature overnight. After the reaction completed, the solvent was removed using a rotary evaporator, and then the resulting **Compound A-Cholesterol** was purified using analytic HPLC equipped with a C18 column. **Compound A-Cholesterol** (0.8 mg, 1.04 μmol, 103.6 μL in DCM) and [$RuCp(CH_3CN)_3PF_6$] (0.45 mg, 1.04 μmol, 103.6 μL in

https://doi.org/10.1021/acsami.5c10736
ACS Appl. Mater. Interfaces 2025, 17, 45569−45578

DCM, 1.0 equiv.) were mixed and stirred at room temperature overnight. After centrifugation, the supernatant was collected and dried under a stream of N_2. The resulting **Ru-Cholesterol catalyst** was used directly in the subsequent experiment (Scheme S3).

Calculation of Yield of NBD-K. We evaluated the catalytic activity of catalysts by calculating the yield of **NBD-K** at each reaction conditions. The quantity of **NBD-K** and **NBD-Alloc** are analyzed using HPLC by comparing the integral area of peaks located at 2.9 and 3.7 min, respectively. Yield of **NBD-K** is calculated as follows:

$$\text{Yield of } \mathbf{NBD\text{-}K} = \frac{A_{\mathbf{NBD\text{-}K}}}{A_{\mathbf{NBD\text{-}K}} + A_{\mathbf{NBD\text{-}Alloc}}}$$

where A is the integral area in HPLC analysis.

Investigation of Ru Catalyst Induced Self-Assembly Property of NBD-Alloc. We dissolved **NBD-Alloc** in PBS buffer and adjusted pH to 7.4; the final concentration is 50 μM. Then we added **Ru−C_{12} catalyst**/**Ru-Cholesterol catalyst** (20 μM) into the samples; after incubating for 30 min and 1, 2, 4, 12, and 24 h, we detected the yield of **NBD-K** by LC-MS. Meanwhile, we tested the self-assembly morphology of formed nanostructures at different time point using TEM images.

Thioflavin T Staining of Nanostructures Formed by NBD-Alloc and Ru−C_{12} catalyst. Thioflavin T was dissolved in PBS at a concentration of 1 mM. Following the addition of Thioflavin T solution to **NBD-Alloc**, the **Ru−C_{12} catalyst** was introduced, and the fluorescence intensity was measured at 485 nm every 10 min for a duration of 24 h. The excitation wavelength was set at 450 nm. The final concentrations of **NBD-Alloc**, **Ru−C_{12} catalyst**, and Thioflavin T were 50, 20, and 10 μM, respectively.

Living Cell Imaging. We used CLSM to investigate the cellular distribution of **NBD-Alloc** in the absence and presence of the **Ru catalyst**. (1) The U2OS, HS-5, MCF-7, and DC2.4 cells were seeded at the CLSM dish (20×10^4 cells, 2 mL) and incubated with culture medium overnight. (2) The cells were incubated with **Ru catalyst** for 30 min at a concentration of 20 μM. (3) After discarding the culture medium containing **Ru catalyst**, we washed cell 3 times using culture medium, then we added **NBD-Alloc** to incubate with cells for another 1 h; the concentration of **NBD-Alloc** in U2OS, HS-5, MCF-7, and DC2.4 cells is 50, 55, 80, and 150 μM, respectively. (4) After washing cells 3 times and staining the cells with membrane deep red tracker and Hoechst 33342 for 30 min, we washed cells with living buffer 3 times, then used CLSM to detect the cellular distribution. (5) As the control experiment, the U2OS, HS-5, MCF-7, and DC2.4 cells were only incubated with **NBD-Alloc** for 1 h; after staining with lysosome/membrane deep red tracker and Hoechst 33342, we washed cells and performed CLSM images.

Investigation of Yield of NBD-K Inside Cells. After incubating different kinds of cells with **NBD-Alloc** in the absence and presence of **Ru catalyst**, we collected culture medium and cell lysate, then freeze-dried the samples and performed LC-MS to calculate yield of **NBD-K** inside cells and in culture medium.

Cellular Distribution of Self-Assemblies within Living Cells by Bio-SEM and Bio-TEM. We incubated cells with **NBD-Alloc** in the absence and presence of **Ru catalyst** for 1 and 2 h, respectively. The **Ru catalyst** was preincubated with cells for 30 min. After collecting cells (1×10^6) using a scraper and washing cells with cell living buffer 3 times, we added 600 μL of a mixture of 2% PFA and 2.5% glutaraldehyde to samples to incubate at 4 °C overnight, then the samples were prepared according to the standard protocol of Bio-SEM and Bio-TEM and observed by SEM and TEM, respectively.

Isolation of $CD8^+$ T Cells from OT1 Mouse. We isolated $CD8^+$ T cells from OT1 mice using a mouse $CD8^+$ T cell isolation kit. The 48-cell plate was coated with mixtures of antimouse CD3 antibody and antimouse CD28 antibody for 2 h, and then we separate the spleen of OT1 mouse and isolate the $CD8^+$ T cells. We detected the purity of $CD8^+$ T cells by using FCM analysis. The cells were cultured for 5 days to perform the following experiment.

Fluorescence Labeling between $CD8^+$ T Cells and B16F10-OVA Cells. B16F10-OVA cells were first incubated with **NBD-Alloc** for 1 h, while $CD8^+$ T cells were incubated with the **Ru−C_{12} catalyst** for 30 min. The concentration of **NBD-Alloc** and **Ru−C_{12} catalyst** is 50 and 20 μM, respectively. After washing each cell type 3 times, B16F10-OVA cells were stained with Hoechst 33342, and $CD8^+$ T cells were stained with a mixture of Hoechst 33342 and a membrane tracker. The two cell types were then coincubated for an additional 0.5, 1, and 2 h, then we performed FCM analysis and CLSM images to observe the percentage of fluorescence labeling cells and cellular distribution of fluorescence. For the control experiment, B16F10-OVA cells were incubated with **NBD-Alloc** for 1 h, while $CD8^+$ T cells received no treatment. Following three washes of both cell types and staining with the respective trackers, the cells were mixed for 1 h and analyzed by FCM and CLSM.

Characterizations. *Liquid Chromatography−Mass Spectrometry (LC-MS).* The synthesized peptides were dissolved in MeOH at a concentration of 0.2−0.5 mg mL^{-1}, and then the purity and molecular weight of samples were detected using LC-MS (Agilent 1260 Infinity). Column: Poroshell 120 EC-C18, 4.6 × 50 mm, 2.7 μm. Mobile phase: solvent A, water with 0.5‰ TFA; solvent B, acetonitrile with 0.5‰ TFA. Gradient: 0−6 min 20−100% B, 6−8 min 100−100% B, 8−10 min 100−20% B over 10 min. Total ion chromatogram (TIC) was detected by ESI mass spectrometry.

Transmission Electron Microscopy (TEM). A 10 μL aliquot of self-assembled nanostructure was placed onto a 200 mesh carbon-coated copper grid, and then the excess samples were removed using a filter paper. We added 10 μL of uranyl acetate (UA) to stain the sample, and the samples were air-dried. The samples were investigated using a Talos L120C TEM (Thermo Fisher, US) operated at 120 kV.

Laser Scanning Confocal Microscopy (CLSM). The peptide treated cells were washed with cell living buffer 3 times, then imaged using Zeiss LSM800 CLSM (Zeiss, Germany).

Biological Scanning Electron Microscopy (Bio-SEM). The fixed cells were washed with cacodylate solution buffer and then fixed by 1% osmic acid. After washing with cacodylate solution and H_2O successively, the cells were dehydrated by 30% ethanol, 50% ethanol, 70% ethanol, 95% ethanol, and 100% ethanol, respectively. The dehydrated cells were placed at glass base under vacuum, then observed by dual-beam scanning electron microscope (Zeiss, Germany).

Biological Electron Microscopy (Bio-EM). The fixed cells were washed with cacodylate solution buffer, then fixed by 1% osmic acid; after washing with cacodylate solution and H_2O, we stained cells with UA. Then the cells were dehydrated by 30% ethanol, 50% ethanol, 70% ethanol, 95% ethanol, and 100% ethanol, successively. After washing cells with 100% acetone, the cells were reacted with acetone and 812 resin (2:1), acetone and 812 resin (1:2), and 812 resin, respectively. The cells were embedded with 812 resins for 48 h at 60 °C, and the embedded cells were fabricated into slices, then observed by Talos L120C TEM (Thermo Fisher, US).

Flow Cytometry (FCM). After isolating $CD8^+$ T cells from OT1 mice, we stained cells with different markers successively, and the cells were filtrated using a nylon membrane, then detected using Analyzer: CytoFLEX LX-5L1 (Beckman, US). A sequential gating strategy was performed to differentiate the $CD8^+$ cells. First FSC-A was plotted vs SSC-A to select the main cell population. Second, FSC-A was plotted vs FSC-H to exclude doublets. Then, live/dead staining was performed to exclude dead cells using Viability Staining Blue. Immune cells were selected using CD45. Among all $CD45^+$ cells, $CD3^+$ cells were regarded as T cells; $CD8^+$ cells were regarded as OT-1 cells.

RESULTS AND DISCUSSION

We sought a biocompatible catalyst by triggering peptide self-assembly in an aqueous solution and cellular conditions. We first synthesized ruthenium derivatives with modification of the C_{12} alkyl chain. After coupling the C_{12} alkyl chain to the hydroxyl group of **Compound A**, the purified product was then complexed with $[RuCp(CH_3CN)_3PF_6]$, yielding the final **Ru−C_{12} catalyst** (Scheme S1, Figures S1−S4, Table S1). We selected an Alloc-modified peptide as a substrate of the

https://doi.org/10.1021/acsami.5c10736
ACS Appl. Mater. Interfaces 2025, 17, 45569−45578

catalyst. We designed the fluorescent catalytic substrate **NBD-Alloc** based on the following principles: WYF acts as the self-assembly motif, facilitating hydrogen bonding and π-π interactions during the self-assembly process. Lysine (K) balances the hydrophilicity of the sequence, while the NBD group serves as a fluorescent reporter to visualize the self-assembly process within cells. The Alloc group functions as a cleavable site that can be selectively removed by an **Ru catalyst**. **NBD-Alloc** was synthesized using SPPS on Rink-amide resin (Scheme S2, Figures S5 and S6).

We next evaluated the **Ru−C_{12}** instructed peptide self-assembly *in vitro* (Figures S7 and S8). We first investigated the catalytic activity of **Ru−C_{12}** at different temperatures and pH values to confirm the optimal reaction conditions. After incubating **NBD-Alloc** with **Ru−C_{12} catalyst** in an aqueous phosphate-buffered saline (PBS, pH 7.4) at 25, 37, 60, and 80 °C for 4 h, the yield of **NBD-K** is detected as 94.8%, 94.8%, 93.9%, and 94.0% (Figures S9 and 1A) by high-performance liquid chromatography (HPLC) analysis, respectively, indicating that the prepared **Ru−C_{12} catalyst** shows the strong applicability at different temperatures. Even at a high temperature, the catalytic activity of the **Ru−C_{12} catalyst** could rarely be influenced. Moreover, the yield of **NBD-K** was 92.0%, 94.8%, 89.3%, and 70.8% at pH 5.0, pH 7.4, pH 9.0, and pH 12.0 after incubating **NBD-Alloc** with **Ru−C_{12} catalyst** for 4 h (25 °C, Figures S10 and 1B), respectively. Compared with the catalytic activity of **Ru−C_{12} catalyst** in the acidic and neutral environment, the **Ru−C_{12} catalyst** shows decreased catalytic activity in the basic environment, which may result from incomplete protonation and worse solubility. Based on the above results, we also investigated the influence of the loading amount of **Ru−C_{12} catalyst** to the yield of **NBD-K**. After incubating **NBD-Alloc** with **Ru−C_{12} catalyst** at a loading amount of 5%, 10%, 20%, 40%, and 80% (25 °C, pH 7.4) for 1 h, the yield of **NBD-K** reached 38.2%, 62.8%, 84.1%, 90.3%, and 94.9%, respectively (Figure S11). The results indicate that the higher loading amount of catalyst can achieve a higher catalytic yield at the same reaction conditions. However, regarding the reaction efficiency and economic efficiency, we selected the loading amount of **Ru−C_{12} catalyst** as 40% and performed the following experiments in PBS buffer (25 °C, pH 7.4).

Time-dependent HPLC analysis reveals that coincubation of **NBD-Alloc** with **Ru−C_{12} catalyst** results in rapid cleavage of the **Alloc** group within 30 min, achieving an average yield of **NBD-K** of 81.0% (Figure 1C). The yield of **NBD-K** gradually gets closer to 100% (Figure 1D) after 4 h. Transmission electron microscopy (TEM) images captured the evolved morphologies of the peptides after adding **Ru−C_{12}**. As shown in Figures 1E and S12, the **NBD-Alloc** forms nanoaggregates at 0 min, transforming into sparse nanofibers after adding **Ru−C_{12} catalyst** for 1 h. With the catalytic ratio of peptides increased, the small nanospheres appeared at 2 h, and the size of the nanospheres gradually became larger in the following time. Finally, it forms nanospheres with an average diameter of 150 nm after incubating **Ru−C_{12}** for 24 h. **NBD-Alloc** alone could self-assemble into mixtures of uniform and crisscrossed nanofibers and aggregates after incubating at PBS buffer for 24 h (Figure S13). Thioflavin T staining of the nanostructures formed by **NBD-Alloc** and the **Ru−C_{12} catalyst** revealed a rapid increase in fluorescence intensity as the incubation time extended from 0 to 1.1 h, peaking at 1.1 h (Figure S14A). Following this initial phase, the fluorescence intensity gradually

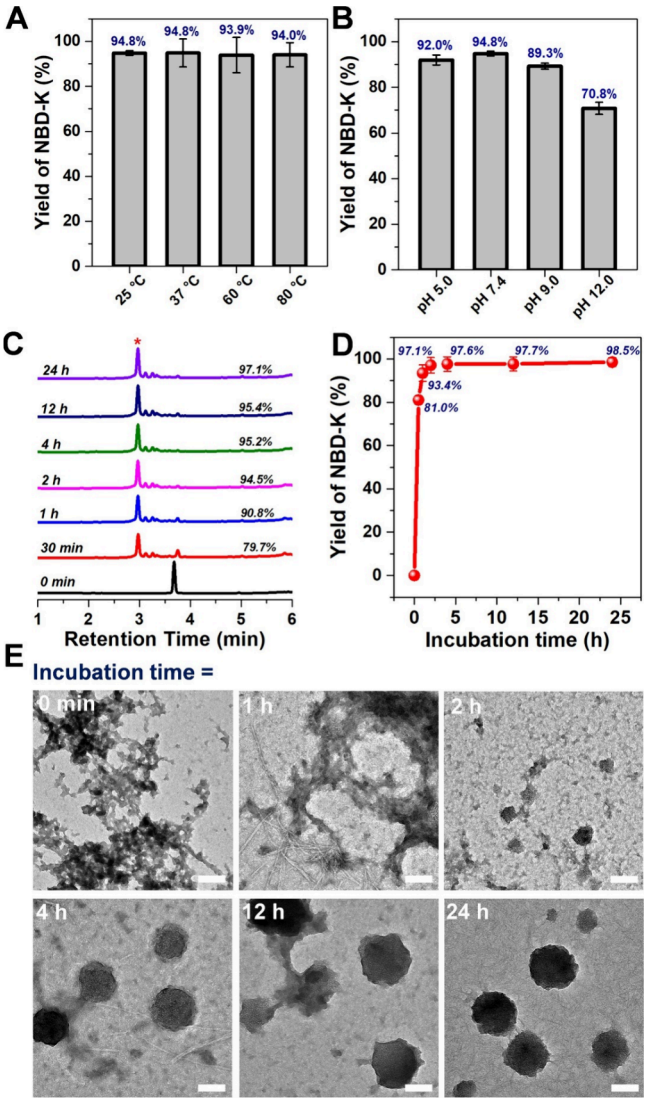

Figure 1. Yield of **NBD-K** from **NBD-Alloc** incubated with **Ru−C_{12} catalyst** for 4 h at different (A) temperatures (pH 7.4) and (B) pHs (25 °C). (C) Time-dependent HPLC analysis and (D) the corresponding yield of **NBD-K** from **NBD-Alloc** incubated with **Ru−C_{12} catalyst** (25 °C, pH 7.4). (E) TEM images of nanostructures formed by **NBD-Alloc** in the presence of **Ru−C_{12} catalyst** at different time points (25 °C, pH 7.4). The concentration of **NBD-Alloc** and **Ru−C_{12} catalyst** is 50 and 20 μM, respectively. The scale bar is 100 nm.

decreased during coincubation, reaching its lowest level at 24 h. CLSM images were acquired at various time points. After 1 h of coincubation, green fluorescence was observed from nanostructures (Figure S14B), indicating the presence of β-sheet structures. By 2 h, the fluorescence intensity had diminished, and aggregates that could not be stained with thioflavin T began to appear. At 6 h, all aggregates were unstained by thioflavin T, suggesting the complete disappearance of β-sheet structures. After 24 h, larger aggregates formed, which also remained unstained. These results indicate that **NBD-Alloc** initially forms β-sheet structures, but prolonged incubation in the presence of the **Ru−C_{12} catalyst** leads to the cleavage of **NBD-Alloc**, disrupting the β-sheet secondary structure. Consequently, the cleavage products self-assemble into alternative nanostructures. The CLSM observations are

https://doi.org/10.1021/acsami.5c10736
ACS Appl. Mater. Interfaces 2025, 17, 45569−45578

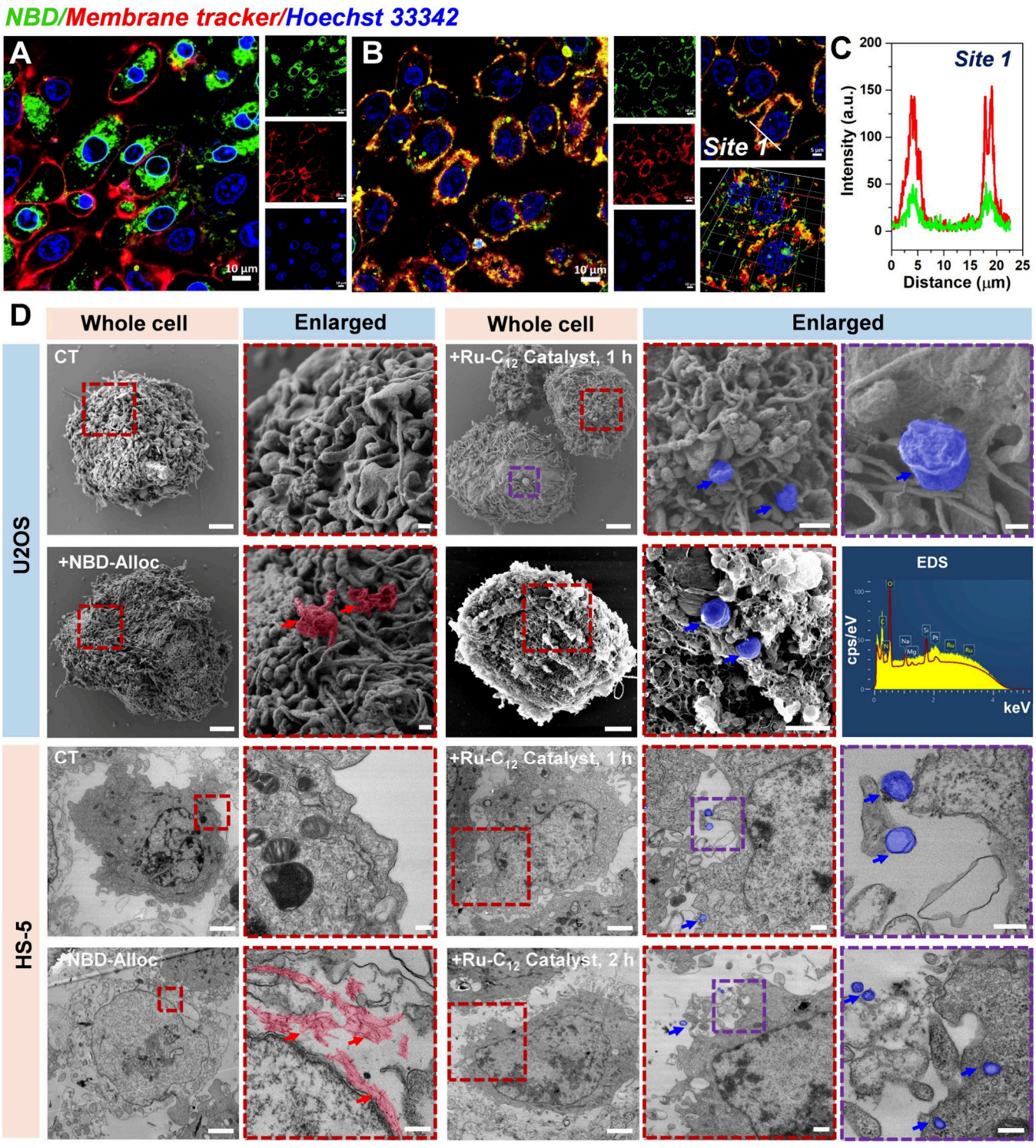

Figure 2. CLSM images and 2D profile of U2OS cells incubated with **NBD-Alloc** in the (A) absence or (B, C) presence of **Ru−C_{12} catalyst** for 1 h. The cells were preincubated with **Ru−C_{12} catalyst** for 30 min. (D) Bio-SEM and Bio-EM images of U2OS cells and HS-5 cells incubated with PBS and **NBD-Alloc** in the absence or presence of **Ru−C_{12} catalyst** for different times. The red and blue arrows indicate the nanofibers and nanospheres, respectively. Scale bar at the first, second, third, fourth, and fifth column is 2 μm, 200 nm, 2 μm, 500 nm, and 200 nm, respectively.

consistent with both the fluorescence intensity measurements and the TEM images, collectively demonstrating that the **Ru−C_{12} catalyst** induces the cleavage of **NBD-Alloc** and a subsequent structural transition from β-sheet-containing nanofibers to β-sheet-free nanospheres. This approach enables control over peptide self-assembly, allowing the formation of different morphologies through the introduction of the **Ru−C_{12} catalyst**. The results demonstrate that we could control peptide self-assembly to achieve different morphologies by introducing the **Ru−C_{12} catalyst**.

To validate the designed concept of controlling transition metal catalyst-mediated peptide self-assembly in living cells, we selected two kinds of cancer cells (human osteosarcoma cells, U2OS; human breast cancer cells, MCF-7) and two kinds of

https://doi.org/10.1021/acsami.5c10736
ACS Appl. Mater. Interfaces 2025, 17, 45569−45578

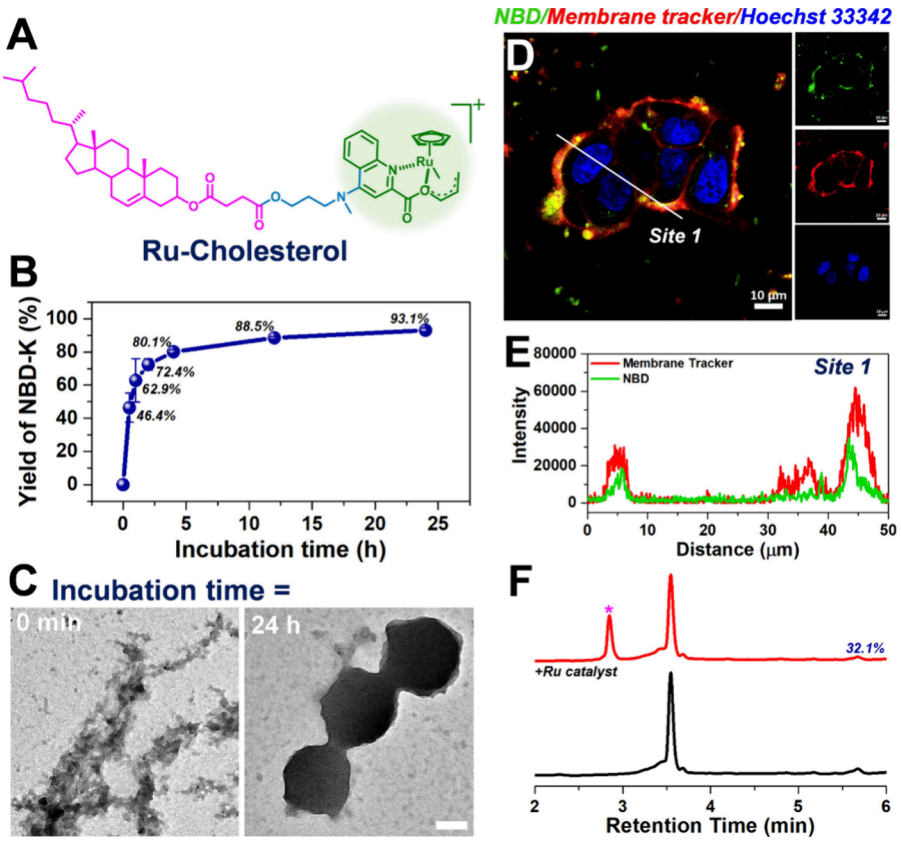

Figure 3. (A) Molecular structure of **Ru-cholesterol catalyst**. (B) The yield of **NBD-K** hydrolyzed from **NBD-Alloc** incubated with **Ru-cholesterol catalyst** at different times (25 °C, pH 7.4). (C) TEM images of nanostructures formed by **NBD-Alloc** in the presence of **Ru-cholesterol catalyst** for 0 min and 24 h. (D) CLSM images, (E) 2D profile, and (F) yield of **NBD-K** in cell lysate of MCF-7 cells incubate with **NBD-Alloc** in the presence of **Ru-cholesterol catalyst** for 1 h. The cells were preincubated with **Ru-cholesterol catalyst** for 30 min. The concentrations of **NBD-Alloc** and **Ru-cholesterol catalyst** in (A–C) are 50 and 20 μM, respectively. Scale bar of TEM images is 100 nm.

normal cells (human bone marrow stromal cells, HS-5; mouse dendritic cells, DC2.4) as model cell lines. We first investigated the cytotoxicity of U2OS cells incubated with **Ru−C_{12} catalyst**. The results showed that **Ru−C_{12} catalyst** exhibited moderate cytotoxicity at higher concentration after 1 and 24 h incubation (Figure S15A). We also evaluated the cytotoxicity of U2OS cells incubated with **NBD-Alloc** in the absence and presence of the **Ru−C_{12}** catalyst. At higher concentration, both groups exhibited cytotoxicity to some extent, with no significant difference between **NBD-Alloc** in the absence and presence of **Ru−C_{12} catalyst** (Figure S15B,C), suggesting that the optimization of abiotic catalyst is necessary in the future. We next investigated the effect of preincubation time of U2OS cells with the **Ru−C_{12} catalyst**. When U2OS cells were preincubated with **Ru−C_{12} catalyst** for 10, 20, or 30 min, followed by incubation with **NBD-Alloc** for an additional 1 h, the yield of **NBD-K** in the cell lysate increased from 16.7% to 40.5% and finally to 63.0% (Figure S16), suggesting that longer preincubation with **Ru−C_{12} catalyst** enhances cellular internalization. Considering the total reaction time, we selected 30 min as the optimal preincubation time with the catalyst. We also evaluated the labeling ratio of the **Ru−C_{12} catalyst** at cells. We collected the culture medium and cell lysate after incubating U2OS cells with the **Ru−C_{12} catalyst** for 30 min (20 μM). We freeze-dried the samples to incubate them with **NBD-Alloc** at a concentration of 50 μM. After comparing the yield of **NBD-K** in culture medium and cell lysate, we estimated that approximately 11.7 μM of the **Ru−C_{12} catalyst** (58.5%) was retained within the cells (Figure S17), demonstrating the high efficiency of our strategy for catalyst internalization. Based on the above results, we investigated the cellular distribution of living cells incubated with **NBD-Alloc** in the absence or presence of the **Ru−C_{12} catalyst**. As shown in Figure 2A, U2OS cells incubated with **NBD-Alloc** displayed strong green fluorescence in the cytoplasm. In contrast, preincubating U2OS cells with **Ru−C_{12} catalyst** for 30 min before adding **NBD-Alloc** results in the green fluorescence distributed on the cell membrane (Figure 2B), with significant overlap between the green fluorescence derived from **NBD-Alloc** and red fluorescence from cell membrane tracker (Figure 2C). Longer incubation times did not significantly alter the cellular distribution of **NBD-Alloc** (Figure S18). The results indicate that the preanchored catalyst could control peptide self-assembly on the cell membrane.

We further performed LC-MS experiments of cells to examine whether the catalytic reaction occurs on the cell membrane. The peaks corresponding to the catalytic product could be observed in the U2OS cell lysate after the treatment with **NBD-Alloc** and **Ru−C_{12} catalyst**, and the yield of **NBD-K** is calculated as 63.0% (Figure S19E). In contrast, the retention time of **NBD-Alloc** remains unchanged in both the culture medium and the cell lysate without preincubation with **Ru−C_{12} catalyst** (Figure S19). Similar results are also observed in the other three kinds of cell lines. Upon incubation of MCF-7 cells, HS-5 cells, and DC2.4 cells with **NBD-Alloc**, green fluorescence was observed in the lysosomes of MC-7 and

https://doi.org/10.1021/acsami.5c10736
ACS Appl. Mater. Interfaces 2025, 17, 45569−45578

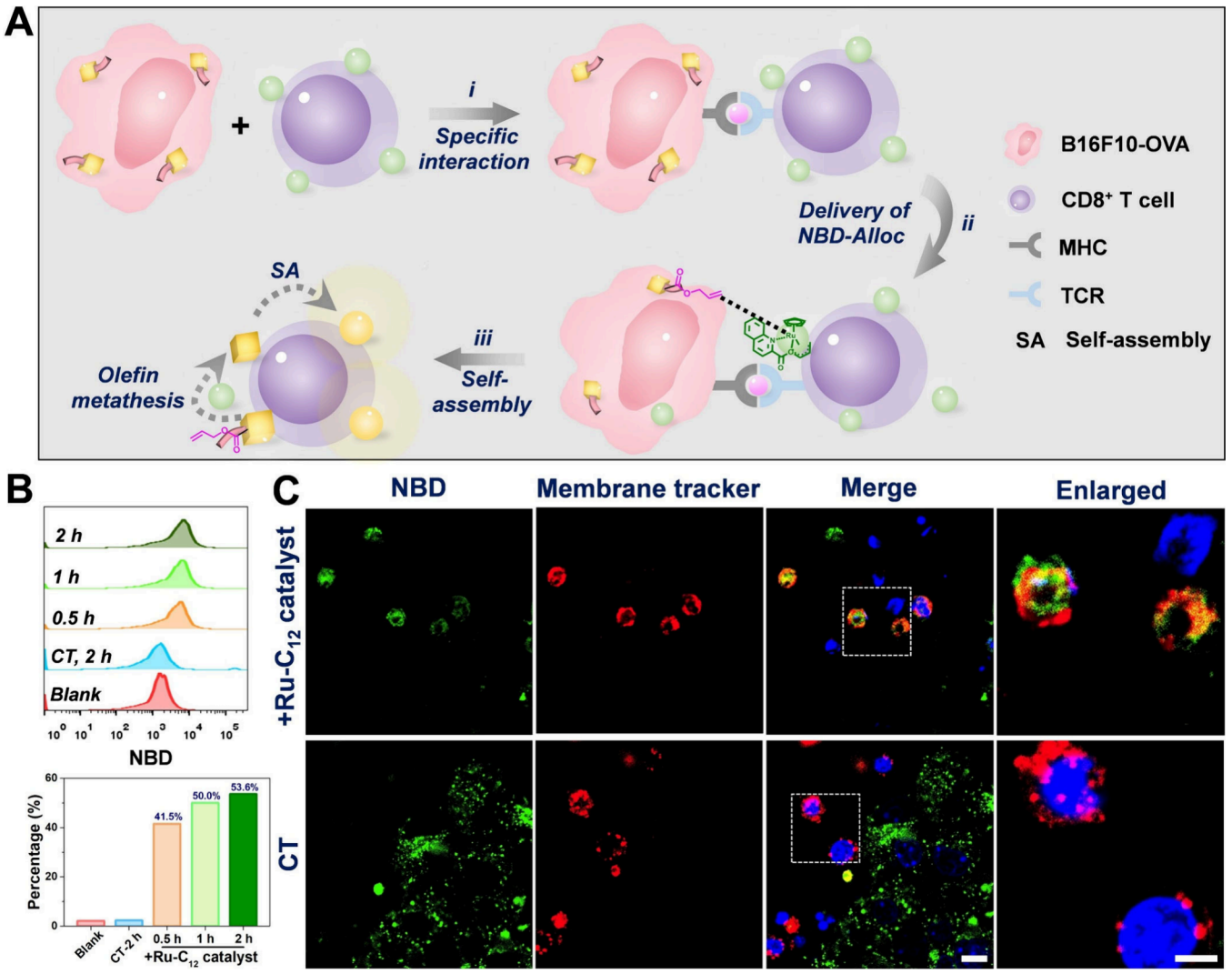

Figure 4. (A) Schematic illustration of **Ru catalyst** mediated fluorescence labeling at the cell membrane between B16F10-OVA and $CD8^+$ T cells. (B) FCM analysis and quantitative results of fluorescent $CD8^+$ T cells incubated with B16F10-OVA cells with different modifications. (C) CLSM images of $CD8^+$ T cells incubated with B16F10-OVA cells for 1 h; these two kinds of cells were preincubated with **Ru−C_{12} catalyst** and **NBD-Alloc** for 30 min and 1 h, respectively. The concentration of **NBD-Alloc** and **Ru−C_{12} catalyst** is 50 and 20 μM, respectively. Scale bar of CLSM images in the first three columns and last column is 10 and 5 μm, respectively.

HS-5 cells, whereas in DC2.4 cells, the fluorescence was predominantly localized to the cytoplasm, which could be demonstrated by the overlap between green fluorescence from the NBD and red fluorescence from the lysosome tracker (Figure S20). However, after preincubating cells with **Ru−C_{12} catalyst**, the green fluorescence could be observed on cell membrane, and the yield of **NBD-K** (Figures S19 and S20) inside cells are 76.4% (MCF-7), 71.8% (HS-5 cells), and 84.2% (DC2.4), respectively, which differ from the zero yield of **NBD-K** observed in the culture medium and cell lysate when not preincubated with the **Ru−C_{12} catalyst**. These encouraging results demonstrate that transition metal catalysts can be introduced into living cells without compromising their catalytic activity, enabling the triggering of peptide self-assembly at the designated cellular location where the catalyst is present while the catalytic reaction does not occur elsewhere.

To examine the catalyst induced **NBD-Alloc** self-assembly on the cell membrane, we employed Bio-SEM and Bio-EM to observe the cells with different treatments. Compared to the untreated U2OS cells (Figure 2D, upper layer), **NBD-Alloc** treated cells exhibit aggregated nanofibers among synapses, and we also observe the appearance of small and irregular spherical nanostructures, which may result from the secretions of cells. After preanchoring the **Ru−C_{12} catalyst** on U2OS cells, **NBD-Alloc**-treated cells showed nanospheres with a diameter of 150 nm on the cell surface. We found the Ru element at the nanospheres-rich region, indicating that the catalyst may participate in the formation of nanospheres. For MCF-7 cells and HS-5 cells treated with **NBD-Alloc**, the nanofibers can be observed inside the cytoplasm. In contrast, the nanospheres were formed at the outer and inner cell membranes when the cells were pretreated with **Ru−C_{12} catalyst** (Figure 2D, lower layer, Figure S21). These results, agreeing with CLSM results, confirm that the preintroduced catalyst can control peptide self-assembly at the confined locations where the catalysts are, and only through preincubation with **Ru−C_{12} catalyst** could the **NBD-Alloc** form uniform nanospheres on the cell membrane.

To validate the generalization of the scaffold of the catalyst, we replaced the alkyl chain with cholesterol, a widely used cell

https://doi.org/10.1021/acsami.5c10736
ACS Appl. Mater. Interfaces 2025, 17, 45569−45578

membrane affiliative motif, resulting in the **Ru-cholesterol catalyst** (Figure 3A, Scheme S3, and Figures S22−S24). Time-dependent HPLC experiments and TEM images demonstrate the ability of **Ru-cholesterol catalyst** to catalyze the cleavage of the **Alloc** group and induce the morphologies transformation from nanoaggregates to uniform nanospheres (Figures 3B and 3C, Figures S25 and S26). CLSM results (Figures 3D and 3E, Figures S27A and S27B) showed that when pretreating MCF-7 (or HS-5 cells) with **Ru-cholesterol catalyst**, the green fluorescence from the hydrolysis product of **NBD-Alloc** exists on the cell membrane rather than inside cells (Figure S20), and the yield of **NBD-K** inside cells are 32.1% and 21.4% (Figures 3F and S27), respectively. Moreover, the successful restriction of peptide self-assembly on the cell membrane mediated by **Ru-cholesterol catalyst** further demonstrates that we could modify the **Ru catalyst** with different targeting groups to achieve peptide self-assembly at desired locations.

The above results showed that the **Ru−C_{12} catalyst** can anchor on the cell membrane, allowing peptide self-assembly restriction on the cell surface. Based on the above results, we consider whether the catalyst and the substrate could orthogonally label two types of cells and transfer molecules from one cell type to another through olefin metathesis. We chose B16F10-OVA and $CD8^+$ T cells as the model cell lines because of the specific interaction between the two kinds of cells (Figure 4A). After collecting $CD8^+$ T cells from OT-1 mice and culturing them for 5 days (Figures S28 and S29), we modified $CD8^+$ T cells with **Ru−C_{12} catalyst** on the cell membrane, and the B16F10-OVA cells were incubated with **NBD-Alloc**, respectively. Co-culturing these two kinds of cells for a certain time, we separated $CD8^+$ T cells, then detected the percentage of cells with fluorescence labeling using FCM. The results indicated that with the increase of coincubation time, the percentage of $CD8^+$ T cells with **NBD-Alloc** labeling increased from 41.5% (0.5 h), 50.0% (1 h), to 53.6% (2 h) (Figure 4B), respectively. However, when we did not preincubate $CD8^+$ T cells with **Ru−C_{12} catalyst**, we could hardly observe the appearance of cells with fluorescence labeling. The results indicate that modification of **Ru−C_{12} catalyst** with $CD8^+$ T cells then coincubation with **NBD-Alloc** labeled B16F10-OVA cells could achieve the fluorescence transfer from B16F10-OVA cells to $CD8^+$ T cells. Furthermore, CLSM images show that after coculturing two kinds of cells for 1 h, the green fluorescence appears on the cell surface of $CD8^+$ T cells, which could overlap with the cell membrane tracker (Figure 4C, upper layer, Figure S30), indicating that the **NBD-Alloc** in B16F10-OVA cells can transfer into the $CD8^+$ T cells and trigger the restricted self-assembly on $CD8^+$ T cell with **Ru−C_{12} catalyst** because of close contact between these two cell lines. As a control, the green fluorescence only appears at the inner cytoplasm and cell membrane of B16F10-OVA cells (Figure 4C, lower layer, Figure S31), and it could not be delivered onto the cell surface of $CD8^+$ T cells without anchoring the catalyst. The delivery of fluorescent molecules may result from three steps (Figure 4A): (i) the specific interactions between MHC and TCR induce the close contact of B16F10-OVA cells and $CD8^+$ T cells; (ii) the close contact between two kinds of cells could induce the diffusion of **NBD-Alloc** in B16F10-OVA cells out of the cytoplasm over time; and (iii) when the **NBD-Alloc** are transferred to $CD8^+$ T cells, it could be restricted on the cell membrane by the anchored **Ru−C_{12} catalyst**, and the green fluorescence could be generated, contributing to the **Ru catalyst** mediated the self-assembly. The results suggest that not only can we control peptide self-assembly at the desired locations of single cells where the catalyst is but we can also achieve the modulation of molecular transfer between two kinds of cell lines.

CONCLUSION

In summary, this work achieved chemically controlling peptide self-assembling on a defined cell location within the living cell by harnessing cellular compatible transition metal, which provides a powerful strategy to create higher-order structures to engineer the cells of interest. This work also suggests that cell-compatible organic catalysts are excellent candidates for triggering molecular self-assembly with rational design. The molecular transfer experiments by the orthogonal labeling of catalysts and substrates on two types of cell lines also indicate that this is a potential strategy for modulating diverse cell−cell interactions.

ASSOCIATED CONTENT

Supporting Information

The Supporting Information is available free of charge at https://pubs.acs.org/doi/10.1021/acsami.5c10736.

Synthetic routes of **Ru catalysts** and **NBD-Alloc**; ^1H NMR spectroscopy, LC-MS, and MALDI-TOF mass spectrometry of synthetic compounds; temperature-dependent, pH-dependent, and catalysts' loading amount-dependent catalytic activity of **Ru−C_{12} catalyst**; TEM images of nanostructures formed by NBD-Alloc; cytotoxicity of Ru−C_{12} catalyst; label ratio of **Ru−C_{12} catalyst** in U2OS cells; CLSM results of living cells incubate with NBD-Alloc; LC-MS of cell lysate and culture medium; Bio-EM images of MCF-7 cells incubate with NBD-Alloc in the absence and presence of **Ru catalyst**; and CLSM images of $CD8^+$ T cells incubated with B16F10-OVA cells with different modifications (PDF)

AUTHOR INFORMATION

Corresponding Authors

Zhaoqianqi Feng − *School of Engineering, Westlake University, Hangzhou, Zhejiang Province 310024, China*; Email: fengzhaoqianqi@westlake.edu.cn

Huaimin Wang − *Westlake Laboratory of Life Sciences and Biomedicine, Hangzhou, Zhejiang Province 310024, China; Department of Chemistry, School of Science, Westlake University, Hangzhou, Zhejiang Province 310024, China*; orcid.org/0000-0002-8796-0367; Email: wanghuaimin@westlake.edu.cn

Authors

Xuejiao Yang − *Westlake Laboratory of Life Sciences and Biomedicine, Hangzhou, Zhejiang Province 310024, China*

Feili Zhang − *School of Engineering, Westlake University, Hangzhou, Zhejiang Province 310024, China*

Bihan Wu − *Department of Chemistry, School of Science, Westlake University, Hangzhou, Zhejiang Province 310024, China*

Juan Liang − *Department of Chemistry, School of Science, Westlake University, Hangzhou, Zhejiang Province 310024, China*

Laicheng Zhou − *Department of Chemistry, School of Science, Westlake University, Hangzhou, Zhejiang Province 310024, China*

Honglei Lu − *Department of Chemistry, School of Science, Westlake University, Hangzhou, Zhejiang Province 310024, China*

Complete contact information is available at: https://pubs.acs.org/10.1021/acsami.5c10736

Author Contributions

The manuscript was written through contributions of all authors. All authors have given approval to the final version of the manuscript.

Notes

The authors declare no competing financial interest.

■ ACKNOWLEDGMENTS

This project was supported by the National Key Research and Development Program of China (2022YFB3808300), the National Natural Science Foundation of China (82272145, 22205183), and the Zhejiang Provincial Natural Science Foundation of China under Grant LY24E030009. This research was supported by Instrumentation and Service Centers for Molecular Science and for Physical Science, respectively, as well as by Biomedical Research Core Facilities at Westlake University.

■ REFERENCES

(1) Whitesides, G. M.; Grzybowski, B. Self-assembly at all scales. *Science* **2002**, *295* (5564), 2418−2421.
(2) Percec, V.; Ungar, G.; Peterca, M. Self-Assembly in Action. *Science* **2006**, *313* (5783), 55−56.
(3) Kushner, D. Self-assembly of biological structures. *Bacteriol. Rev.* **1969**, *33* (2), 302−345.
(4) Yang, Z.; Liang, G.; Xu, B. Enzymatic hydrogelation of small molecules. *Acc. Chem. Res.* **2008**, *41* (2), 315−326.
(5) Feng, Z.; Zhang, T.; Wang, H.; Xu, B. Supramolecular catalysis and dynamic assemblies for medicine. *Chem. Soc. Rev.* **2017**, *46* (21), 6470−6479.
(6) Gao, J.; Zhan, J.; Yang, Z. Enzyme-instructed self-assembly (EISA) and hydrogelation of peptides. *Adv. Mater.* **2020**, *32* (3), 1805798.
(7) Chagri, S.; Ng, D. Y. W.; Weil, T. Designing bioresponsive nanomaterials for intracellular self-assembly. *Nat. Rev. Chem.* **2022**, *6* (5), 320−338.
(8) Kim, J.; Lee, S.; Kim, Y.; Choi, M.; Lee, I.; Kim, E.; Yoon, C. G.; Pu, K.; Kang, H.; Kim, J. S. In situ self-assembly for cancer therapy and imaging. *Nat. Rev. Mater.* **2023**, *8* (11), 710−725.
(9) Liang, G.; Ren, H.; Rao, J. A biocompatible condensation reaction for controlled assembly of nanostructures in living cells. *Nat. Chem.* **2010**, *2* (1), 54−60.
(10) He, P.-P.; Li, X.-D.; Wang, L.; Wang, H. Bispyrene-based self-assembled nanomaterials: in vivo self-assembly, transformation, and biomedical effects. *Acc. Chem. Res.* **2019**, *52* (2), 367−378.
(11) Pires, R. A.; Abul-Haija, Y. M.; Costa, D. S.; Novoa-Carballal, R.; Reis, R. L.; Ulijn, R. V.; Pashkuleva, I. Controlling cancer cell fate using localized biocatalytic self-assembly of an aromatic carbohydrate amphiphile. *J. Am. Chem. Soc.* **2015**, *137* (2), 576−579.
(12) Boekhoven, J.; Hendriksen, W. E.; Koper, G. J.; Eelkema, R.; van Esch, J. H. Transient assembly of active materials fueled by a chemical reaction. *Science* **2015**, *349* (6252), 1075−1079.
(13) Versluis, F.; van Esch, J. H.; Eelkema, R. Synthetic self-assembled materials in biological environments. *Adv. Mater.* **2016**, *28* (23), 4576−4592.
(14) Maruyama, T.; Restu, W. K. Intracellular self-assembly of supramolecular gelators to selectively kill cells of interest. *Polym. J.* **2020**, *52* (8), 883−889.
(15) Lock, L. L.; Reyes, C. D.; Zhang, P.; Cui, H. Tuning cellular uptake of molecular probes by rational design of their assembly into supramolecular nanoprobes. *J. Am. Chem. Soc.* **2016**, *138* (10), 3533−3540.
(16) Onogi, S.; Shigemitsu, H.; Yoshii, T.; Tanida, T.; Ikeda, M.; Kubota, R.; Hamachi, I. In situ real-time imaging of self-sorted supramolecular nanofibres. *Nat. Chem.* **2016**, *8* (8), 743−752.
(17) Ai, X.; Ho, C. J. H.; Aw, J.; Attia, A. B. E.; Mu, J.; Wang, Y.; Wang, X.; Wang, Y.; Liu, X.; Chen, H.; et al. In vivo covalent cross-linking of photon-converted rare-earth nanostructures for tumour localization and theranostics. *Nat. Commun.* **2016**, *7* (1), 10432.
(18) Ling, X.; Tu, J.; Wang, J.; Shajii, A.; Kong, N.; Feng, C.; Zhang, Y.; Yu, M.; Xie, T.; Bharwani, Z.; et al. Glutathione-responsive prodrug nanoparticles for effective drug delivery and cancer therapy. *ACS Nano* **2019**, *13* (1), 357−370.
(19) Kim, S.; Chae, J.-B.; Kim, D.; Park, C.-W.; Sim, Y.; Lee, H.; Park, G.; Lee, J.; Hong, S.; Jana, B.; et al. Supramolecular Senolytics via Intracellular Oligomerization of Peptides in Response to Elevated Reactive Oxygen Species Levels in Aging Cells. *J. Am. Chem. Soc.* **2023**, *145* (40), 21991−22008.
(20) Hai, Z.; Li, J.; Wu, J.; Xu, J.; Liang, G. Alkaline phosphatase-triggered simultaneous hydrogelation and chemiluminescence. *J. Am. Chem. Soc.* **2017**, *139* (3), 1041−1044.
(21) Wang, X.; Wang, Q. Enzyme-laden bioactive hydrogel for biocatalytic monitoring and regulation. *Acc. Chem. Res.* **2021**, *54* (5), 1274−1287.
(22) Song, Y.; Li, M.; Song, N.; Liu, X.; Wu, G.; Zhou, H.; Long, J.; Shi, L.; Yu, Z. Self-amplifying assembly of peptides in macrophages for enhanced inflammatory treatment. *J. Am. Chem. Soc.* **2022**, *144* (15), 6907−6917.
(23) Yan, R.; Hu, Y.; Liu, F.; Wei, S.; Fang, D.; Shuhendler, A. J.; Liu, H.; Chen, H.-Y.; Ye, D. Activatable NIR fluorescence/MRI bimodal probes for in vivo imaging by enzyme-mediated fluorogenic reaction and self-assembly. *J. Am. Chem. Soc.* **2019**, *141* (26), 10331−10341.
(24) Li, J.; Kong, H.; Huang, L.; Cheng, B.; Qin, K.; Zheng, M.; Yan, Z.; Zhang, Y. Visible light-initiated bioorthogonal photoclick cycloaddition. *J. Am. Chem. Soc.* **2018**, *140* (44), 14542−14546.
(25) Shi, H.; Kwok, R. T.; Liu, J.; Xing, B.; Tang, B. Z.; Liu, B. Real-time monitoring of cell apoptosis and drug screening using fluorescent light-up probe with aggregation-induced emission characteristics. *J. Am. Chem. Soc.* **2012**, *134* (43), 17972−17981.
(26) Streu, C.; Meggers, E. Ruthenium-induced allylcarbamate cleavage in living cells. *Angew. Chem., Int. Ed.* **2006**, *45* (34), 5645.
(27) Sánchez, M. I.; Penas, C.; Vázquez, M. E.; Mascareñas, J. L. Metal-catalyzed uncaging of DNA-binding agents in living cells. *Chem. Sci.* **2014**, *5* (5), 1901−1907.
(28) Jeschek, M.; Reuter, R.; Heinisch, T.; Trindler, C.; Klehr, J.; Panke, S.; Ward, T. R. Directed evolution of artificial metalloenzymes for in vivo metathesis. *Nature* **2016**, *537* (7622), 661−665.
(29) Zhang, L.; Wang, P.; Zhou, X.-Q.; Bretin, L.; Zeng, X.; Husiev, Y.; Polanco, E. A.; Zhao, G.; Wijaya, L. S.; Biver, T.; et al. Cyclic ruthenium-peptide conjugates as integrin-targeting phototherapeutic prodrugs for the treatment of brain tumors. *J. Am. Chem. Soc.* **2023**, *145* (27), 14963−14980.
(30) Zhao, Z.; Tao, X.; Xie, Y.; Lai, Q.; Lin, W.; Lu, K.; Wang, J.; Xia, W.; Mao, Z. W. In Situ Prodrug Activation by an Affibody-Ruthenium Catalyst Hybrid for HER2-Targeted Chemotherapy. *Angew. Chem., Int. Ed.* **2022**, *134* (26), No. e202202855.
(31) Nasibullin, I.; Smirnov, I.; Ahmadi, P.; Vong, K.; Kurbangalieva, A.; Tanaka, K. Synthetic prodrug design enables biocatalytic activation in mice to elicit tumor growth suppression. *Nat. Commun.* **2022**, *13* (1), 39.
(32) Tomás-Gamasa, M.; Martínez-Calvo, M.; Couceiro, J. R.; Mascareñas, J. L. Transition metal catalysis in the mitochondria of living cells. *Nat. Commun.* **2016**, *7* (1), 12538.

(33) James, C. C.; de Bruin, B.; Reek, J. N. Transition metal catalysis in living cells: progress, challenges, and novel supramolecular solutions. *Angew. Chem., Int. Ed.* **2023**, *62* (41), No. e202306645.

https://doi.org/10.1021/acsami.5c10736
ACS Appl. Mater. Interfaces 2025, 17, 45569−45578